AIAA JOURNAL
Vol. 44, No. 3, March 2006

High-Order Discontinuous Galerkin Discretizations for Computational Aeroacoustics in Complex Domains

Ioannis Toulopoulos*
University of Athens, Athens, Greece
and
John A. Ekaterinaris†
University of Patras, Patras, Greece

Discontinuous Galerkin discretization is applied for the numerical solution of the linearized Euler equations governing propagation of small-amplitude acoustic disturbances. Second-, fourth-, and sixth-order-accurate numerical solutions are obtained for domain discretizations with triangular elements. In addition, discretizations with quadrilateral unstructured meshes are obtained with second- and fourth-order accuracy. Detailed comparisons with exact solutions and accuracy tests are carried out with results obtained for a pressure pulse propagation and reflection from a solid surface. It is demonstrated that for triangular meshes the numerical solutions show grid convergence according to the order of accuracy used for the discretization. The versatility of the method to obtain accurate predictions in complex geometries is demonstrated with the results obtained for sound scattering from a single cylinder and two cylinders.

I. Introduction

THE discontinuous Galerkin (DG) method is applied for the numerical solution of the linearized Euler equations that describe sound propagation in computational aeroacoustics (CAA). The main advantage of using the linearized Euler equations in practical calculations of sound propagation is computational efficiency. The intensity of sound sources, such as vortex noise, broadband turbulence noise, and impulsive noise, can be captured only with the numerical solution of the computationally intensive, nonlinear, viscous, compressible flow equations. However, propagation of the generated acoustic waves away from sources and other important effects, such as scattering from solid surfaces, can be accurately obtained from the linearized Euler equations. The linearized Euler equations, from a numerical point of view, encompass many essential features of the inviscid and viscous flow governing equations. Therefore, it is desirable to obtain predictions of sound generation and propagation with the same numerical method in different domains, for example, noise source capturing with direct numerical simulation or large-eddy simulation (LES), and for propagation away from the sources using the linearized Euler equations.

Compared to computational fluid dynamics, higher-order accuracy both in space and time is required for CAA in order to minimize dissipation and dispersion errors. In the last few years, several high-order-accurate finite difference methods[1–4] found widespread application in CAA. These methods were applied in simple Cartesian-type domains and more complex domains through the use of generalized coordinate transformations. For highly accurate computations in three dimensions, extreme caution is required for the computation of metric quantities[5] that appear in the generalized coordinate transformations in order to preserve the high order of spatial accuracy provided by finite differences. Application of boundary conditions that guarantee the overall high order of accuracy of the method for body-fitted curvilinear meshes is far from trivial.[6] Use of multiblock discretizations of complex domains often results into grid singularities[7] that require special treatment in order to preserve the high order of accuracy needed in CAA calculations. On the other hand, domain decomposition[5] often used for parallelization requires overlap in order to ensure that the high-order accuracy of the interior scheme is retained at the interfaces of the domains.

Subsonic flow numerical solutions with central-difference schemes require some form of numerical smoothing to suppress growth of spurious solutions as a result of unresolvable and parasitic modes, nonlinear interactions, and inaccuracies in boundary conditions. Explicit filtering[8] of the computed solutions with spectral-type filters[1,8] was used to overcome these difficulties. Application of these filters is often necessary for complex domain CAA computations with the linearized equations to suppress oscillations from computational boundaries, parasitic modes, and insufficient spatial resolution. Application of spectral-type filters for complex geometry multidomain computations is not straightforward.

Sound propagation for high-speed flows with discontinuities[4] requires use of shock-capturing methods. For these cases the finite difference weighed essentially nonoscillatory (WENO) schemes[9–11] appear to be an attractive candidate. WENO schemes include, however, a diffusive part, which for high-order WENO approximations is very low. Therefore, applicability of WENO finite difference methods to highly accurate CAA computations must be carefully evaluated.[3] It was shown[12] that high-order (seventh or higher) WENO schemes have satisfactory performance in aeroacoustics.

Unstructured grid methods[13–15] that overcome some problems associated with discretizations of complex domains can also be used in CAA. Preservation of high-order accuracy in finite volume methods[13] is computationally intensive.[15] The recently proposed spectral volume method[15] and the DG method[14] overcome the shortcomings of high-order finite volume methods. The DG method appears to offer certain advantages over the spectral volume method because it is highly local and easy to parallelize as the spectral volume method. In addition, in contrast to the spectral volume that requires complex subdivisions, the DG method is straightforward to extend to three dimensions using the available finite element framework and possible to apply for viscous flow computations.[16] Furthermore, the DG method is suitable high-order-accurate discretizations of complex domains with triangular

---

Presented as Paper 2004-0522 at the 42nd Aerospace Sciences Meeting, Reno, NV, 5–8 January 2004; received 4 October 2004; revision received 26 July 2005; accepted for publication 10 September 2005.

*Graduate Student, Department of Mathematics; currently at P.O. Box 1527, Institute of Applied and Computational Mathematics, FORTH, 71110 Heraklion, Greece; toulioa@iacm.forth.gr.

†Professor, Mechanical and Aerospace Engineering; currently at P.O. Box 1527, Institute of Applied and Computational Mathematics, FORTH, 71110 Heraklion, Greece; ekaterin@iacm.forth.gr. Associate Fellow AIAA.

or quadrilateral elements and can preserve high order of accuracy in distorted meshes and meshes with hanging nodes that can result from local grid refinement.[17] The systematic study of Ref. 18 concluded that anistropic grids offer, in fact, an advantage for wave propagation. It was also shown[19] that for space discretization with a basis of order k the spatial dispersion error is of order $2k + 3$ and the spatial dissipation error is of order $2(k + 1)$. A low computing cost, quadrature-free DG method for CAA with triangular meshes, presented by Atkins and Shu,[20] showed very good performance for test benchmark problems. The quadrature-free method was recently implemented in Ref. 21 for quadrilateral or hexahedral meshes. In this work, we use more general polynomial bases with the objective to make possible three-dimensional, mixed-type CAA–LES solutions in the same numerical framework using a unified DG discretization for source capturing in the LES region and acoustic disturbance propagation in the CAA region.

Application of the DG finite element method to linear CAA, which is a simple multidimensional example of hyperbolic conservation laws, is demonstrated for problems with exact solutions that allow the studying of convergence with the grid size and the estimation of the order of accuracy of the space discretization. High-order polynomial representations (up to fifth order) of the approximate solution within the elements are used. The accuracy of the DG method is demonstrated for triangular and arbitrary shape quadrilateral elements. Comparisons of computed solutions with benchmark test problems are shown, and grid convergence to the desired order of accuracy is demonstrated. Finally, solutions for more complex domains are presented. This paper is organized as follows. The governing equations, the DG method for their spatial discretization, and the boundary conditions used in the calculations are presented first. Sufficient implementation details for the numerical approximation of various terms in the mathematical formulation are given. In the results section, the accuracy of the method is evaluated for benchmark problems, and the suitability of the DG method for CAA in complex domains is demonstrated.

II. Governing Equations

The linearized Euler equations are obtained from the full nonlinear equations governing inviscid compressible flow after linearization for the small-amplitude acoustic disturbances.[22] The two-dimensional linearized Euler equations governing propagation of small-amplitude acoustic-type disturbances in the presence of freestream $\boldsymbol{M}_\infty = (M_x, M_y)$ are

$$\frac{\partial \boldsymbol{q}}{\partial t} + \frac{\partial \boldsymbol{F}}{\partial x} + \frac{\partial \boldsymbol{G}}{\partial y} = S$$

$$\boldsymbol{q} = \begin{bmatrix} u \\ v \\ p \end{bmatrix}, \qquad \boldsymbol{F} = \boldsymbol{A}\boldsymbol{q}, \qquad \boldsymbol{A} = \begin{bmatrix} M_x & 0 & 1 \\ 0 & M_x & 0 \\ 1 & 0 & M_x \end{bmatrix}$$

$$\boldsymbol{G} = \boldsymbol{B}\boldsymbol{q}, \qquad \boldsymbol{B} = \begin{bmatrix} M_y & 0 & 0 \\ 0 & M_y & 1 \\ 0 & 1 & M_y \end{bmatrix}, \qquad S = \begin{bmatrix} 0 \\ 0 \\ p_0 \end{bmatrix} \quad (1)$$

where $\boldsymbol{q}$ is the solution variable vector for the acoustic velocities and pressure; $\boldsymbol{F}$, $\boldsymbol{G}$ are the flux vectors; and $S(x, y; t)$ is a source term, which can contain an initial condition of a pressure disturbance $p_0 = p_0(x, y)$, or a time-varying acoustic pressure excitation of the form $p_0 = p_0(x, y)\sin(\omega t)$. The acoustic density ρ satisfies an equation identical to the equation for the variation of pressure and can be omitted.

III. Temporal Scheme

Time marching of the nonlinear or linearized equations, Eq. (1), can be performed with implicit methods.[23] More recently,[24] steady-state solutions with the DG method were obtained using p-type multigrid acceleration, on a fixed triangular mesh and successive solutions during the cycle with zeroth-, first-, second-, and third-order polynomials. The objective of this work is to obtain time-accurate solutions; therefore, the third- or fourth-order-accurate Runge–Kutta method should be used for explicit time marching. For aeroacoustic computations, time accuracy and the diffusion introduced by the numerical method are important for long time integration. It was shown that a significant increase in performance for long time integration might be obtained with optimized methods.[25,26] In this work, the total-variation-diminishing (TVD) Runge–Kutta method of Ref. 27 is used. This method is TVD in the sense that the temporal operator itself does not increase the total variation of the solution. The TVD property of the time-integration scheme might not be important for linear problems. It plays, however, an important role for time marching of nonlinear hyperbolic problems that use DG space discretizations.

Let $Q_t = R(Q)_e$ be the semidiscrete form of Eq. (1), where R is the spatial discretization for the right-hand-side operator of Eq. (1) $R = -(F_x + G_y)$, to be discussed in the next section. The third-order-accurate TVD Runge–Kutta (RK3) method[27] used for time marching is as follows:

$$\begin{aligned} Q^{(1)} &= Q^n + \Delta t R\big(Q^{(n)}\big) \\ Q^{(2)} &= \tfrac{3}{4} Q^n + \tfrac{1}{4} Q^{(1)} + \tfrac{1}{4} \Delta t R\big(Q^{(1)}\big) \\ Q^{n+1} &= \tfrac{1}{3} Q^n + \tfrac{2}{3} Q^{(2)} + \tfrac{2}{3} \Delta t R\big(Q^{(2)}\big) \end{aligned} \quad (2)$$

IV. Space Discretization

The DG method is briefly described in this section. Further information and mode details can be found in the original references[28–30] and the review articles of Ref. 14. For each time $t \in [0, T]$ the approximate solution q_h of the governing equations in conservation law form, $\partial_t \boldsymbol{q} + \nabla \cdot \boldsymbol{F}(\boldsymbol{q}) = 0$, is sought in the finite element space V_h:

$$\boldsymbol{V}_h = \big\{ v_h \in \boldsymbol{L}^\infty(\Omega) : v_h/_K \in \boldsymbol{V}(\boldsymbol{K}), \forall \boldsymbol{K} \in T_h \big\} \quad (3)$$

where $\boldsymbol{T}_h$ is a discretization of the domain Ω using triangular or quadrilateral elements and $\boldsymbol{V}(\boldsymbol{K})$ is the local space that contains the collection of polynomials up to degree k. The weak formulation of the governing equations is

$$\frac{\mathrm{d}}{\mathrm{d}t} \int_K \boldsymbol{q}(x, t) v(x)\,\mathrm{d}x = -\sum_{e \in \partial K} \int_e \boldsymbol{F}(\boldsymbol{q}(x, t)) \cdot \boldsymbol{n}_{e,K} v(x)\,\mathrm{d}\Gamma + \int_K \boldsymbol{F}(\boldsymbol{q}(x, t)) \cdot \nabla(v(x))\,\mathrm{d}x \quad (4)$$

where $v(x)$ is any sufficiently smooth function and $\boldsymbol{n}_{e,K}$ denotes the outward, unit normal to the face or edge e.

The mass matrix integral at the left-hand side of Eq. (4) is evaluated numerically using Gauss–Radau integration rules. The integrals on the right-hand side of Eq. (4) are evaluated using quadrature rules as follows:

$$\int_e F(q(x, t)) \cdot \boldsymbol{n}_{e,K} v(x)\,\mathrm{d}\Gamma \approx \sum_{l=1}^{L} \psi_l F(q(x_{\mathrm{el}}, t)) \cdot \boldsymbol{n}_{e,K} v(x_{\mathrm{el}}) |e| \quad (5)$$

$$\int_K F(q(x, t)) \cdot \nabla(v(x))\,\mathrm{d}x \approx \sum_{j=1}^{J} \omega_j F(q(x_{Kj}, t)) \cdot \nabla(v(x_{Kj})) |K| \quad (6)$$

The line (surface in three dimensions) integrals of Eq. (5) are computed using appropriate high-order Gaussian quadrature. For example, for a third-order polynomial basis a quadrature rule that integrates exactly at least sixth-order polynomial is used.

The data are assumed discontinuous across the interfaces of the continuous domain, and at each interface two values are available. Therefore, the flux $F[q(x, t)] \cdot \boldsymbol{n}_{e,K} v(x)$ is replaced by a suitable numerical flux $\tilde{F}_{e,K}(x, t)$ for the approximate solution q_h, and the test function $\upsilon_h \in V(K)$. Using $\tilde{F}_{e,K}(x, t)$ in Eqs. (4) and (5), the approximate solution q_h is obtained from

$$\frac{\mathrm{d}}{\mathrm{d}t}\int_K q_h(x,t)\upsilon_h(x)\,\mathrm{d}x = \sum_{j=1}^{J}\omega_j F[q_h(x_{Kj},t)]\cdot\nabla[\upsilon_h(x_{Kj})]|K| - \sum_{e\in\partial K}\sum_{l=1}^{L}\psi_l \tilde{F}_{e,K}(x_{\mathrm{el}},t)\upsilon_h(x_{\mathrm{el}})|e| \qquad \forall\upsilon_h \in V(K), \qquad \forall K \in T_h \tag{7}$$

where time advancement of Eq. (7) is performed with the third-order-accurate Runge–Kutta method.

The major difference of the DG formulation with a standard Galerkin finite element method is that the expansion in each element is local without any continuity across the element boundaries. Communication between the elements in the DG formulation is achieved through the interface numerical flux. The value of the numerical flux $\tilde{F}_{e,k}(x, t)$ at the edge of the boundary of the element K depends on two values of the approximate solution: one from the interior (right) of the element K, $q^R = q_h[x^{\mathrm{int}(K)}, t]$, and the other from the exterior (left) of the element K, $q^L = q_h[x^{\mathrm{ext}(K)}, t]$. Any consistent, conservative exact or approximate Riemman solver can be used to obtain the numerical flux $\tilde{F}_{e,K}\{q[x^{\mathrm{int}(k)}, t], q[x^{\mathrm{ext}(k)}, t]\}$ as follows:

$$\tilde{F}_{e,K}(q^L, q^R) = \tfrac{1}{2}\left[F(q^L)\cdot\boldsymbol{n}_{e,K} + F(q^R)\cdot\boldsymbol{n}_{e,K} - F^*(q^L, q^R)\right] \tag{8}$$

where $F^*(q^L, q^R)$ is the dissipative part of the numerical flux. The computationally efficient local Lax–Friedrichs flux used is F. The flux is split as $F = F^+ + F^-$, where $F^\pm = F + \alpha q$, where $\alpha = \lambda$ and λ is the maximum eigenvalue of the flux Jacobian. For the linearized Euler equations, the eigenvalues are constant, and the derivatives are continuous for the nonlinear case; however, to obtain continuous higher derivatives, $\alpha = \sqrt{(\varepsilon^2 + \lambda^2)}$ with $\varepsilon = 0.05$.

A. Boundary Conditions

The following boundary conditions were used for the aeroacoustic computations. At the solid wall or the symmetry line a fictitious cell was used. The value of the velocity was specified so that the normal to the wall flux is zero and the velocity is tangent to the surface. The condition of zero-velocity components normal to the surface $\boldsymbol{u}\cdot\boldsymbol{n} = 0$, combined with the first and second of Eqs. (1), implies that $\nabla p\cdot\boldsymbol{n} = 0$, where $\boldsymbol{n}$ is the outward normal to the surface vector. The solid wall boundary condition (shown schematically in Fig. 1) is applied through the use of a fictitious cell.

At the outflow boundaries the following radiation boundary condition[2] was used:

$$\left(\frac{1}{V_r}\frac{\partial}{\partial t} + \cos\vartheta\frac{\partial}{\partial x} + \sin\vartheta\frac{\partial}{\partial y} + \frac{1}{2r}\right)\begin{bmatrix} u \\ \upsilon \\ p \end{bmatrix} = 0 \tag{9}$$

where $V_r = u\cos\vartheta + \upsilon\sin\vartheta$, r is the distance from the source $r = [(x - x_s)^2 + (y - y_s)^2]^{1/2}$, and ϑ is the angle between the horizontal and the line between the boundary point and the source. The implementation of the radiation boundary condition[2] is similar to the wall boundary condition implementation with the difference that the values of the variables in the fictitious cell are obtained from the radiation boundary condition of Eq. (9).

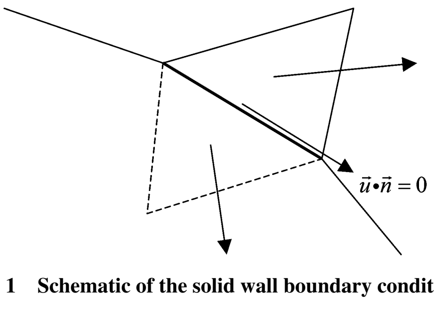

Fig. 1 Schematic of the solid wall boundary condition.

B. Triangular Element Bases

For the general nonlinear case, the order of accuracy of the DG method (see Ref. 14 and references therein) is at least $k + \frac{1}{2}$ if polynomials of degree at most k are used as basis functions. Furthermore, it was shown[14] that for linear problems for canonical semiuniform triangular grids the order of accuracy is $(k + 1)$. For simplicity in the rest of this paper, the method is called $(k + 1)$th-order accurate if the basis functions are polynomials of degree at most k.

The approximate solution within each element is expanded in a series of local bases functions (polynomials) as follows:

$$q_h(x, y, t) = \sum_{j=1}^{d} c_j(t) P_j^k(x, y) \tag{10}$$

where $c_j(t)$, $j = 1, 2, \ldots, d$ are expansion coefficients or degrees of freedom for each element, to be computed at each time step, and $P_j^k(x, y)$ are polynomial bases of degree k the most. The base of polynomials P_j^k, $j = 1, \ldots, d$ of Eq. (10) has dimension

$$d = \binom{n+k}{k} = \frac{(n+k)!}{n!k!} \tag{11}$$

where k is the order of the polynomial $P^k_{j=1,\ldots,d}$ and n is the spatial dimension of the problem [for $n = 2$ in the present work $d = (k + 1)(k + 2)/2$]. It can be seen that in three dimensions the third-order basis includes 20 polynomials and the fifth-order basis includes 56 polynomials. It appears, therefore, that for realistic, three-dimensional problems it could be very intensive computationally to achieve global accuracy higher that fourth order. Therefore, for three-dimensional applications higher order of accuracy (higher than fourth) must be used only locally in regions with steep gradients through a p-adaptive mechanism.

The expansion of the approximate solution of Eq. (10) can be performed with nodal or modal bases.[31,32] Examples of modal bases are the nonorthogonal power base (obtained from Pascal's triangle for tensor product quadrilateral expansions) and the widely used orthogonal Legendre polynomial base,[32] which are special case of the Jacobi polynomials. In most of the computations, third- and fifth-order nodal (Lagrange) polynomial bases were used. These bases are nonorthogonal, but the inverse of the mass matrix can be stored and used during the computations. For high-order expansions with nonorthogonal bases, the mass matrix condition number plays an important role because large condition numbers cause loss of accuracy because of round-off errors. The mass matrix condition number for the equidistant Lagrange bases up to degree $k = 6$ is very close to the optimal condition number $\kappa_{\mathrm{opt}} = \kappa_{\mathrm{orth}} = 2k - 1$ of the modal, orthogonal Legendre base. In contrast, the condition number of the hierarchical power basis grows as 10^k.

The main advantage from the use of the nodal bases is computational efficiency that is gained from the efficient evaluation of the numerical flux line integral

$$\sum_{e\in\partial K}\sum_{l=1}^{L}\psi_l\tilde{F}_{e,K}(x_{\mathrm{el}}, t)\upsilon_h(x_{\mathrm{el}})|e|$$

in Eq. (7). For a nodal base, only few of the total number of the polynomials, $d = (k + 1)(k + 2)/2$, in the base are nonzero on each edge. For example, a fifth-order nodal base includes $d = 6 \times 7/2 = 21$ polynomials, but only six of these polynomials are nonzero on each edge. For the modal orthogonal base, all of the polynomials are nonzero on the edges, and they are involved in the evaluation of the line integral of the numerical flux. As a result, the computing cost for the evaluation of the line integral in Eq. (7) increases. The polynomials of the nodal (Lagrange) and orthogonal modal (Jacobi) polynomial bases used in this work are given next.

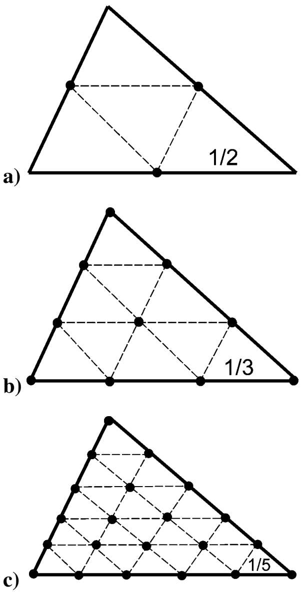

Fig. 2 Nodal points for P^1, P^3, and P^5 polynomial bases on triangular meshes: a) first-order polynomial basis function, b) third-order polynomial basis function, and c) fifth-order polynomial basis function.

1. *First-Order Polynomials*

The following orthogonal first-order basis, $P^1_{j=1,2,3}$, achieves second-order accuracy:

$$P^1_1 = 1 - 2y, \quad P^1_2 = 2x + 2y - 1, \quad P^1_3 = 1 - 2x \tag{12}$$

Each of these polynomials (Fig. 2) takes unit value at one node, located in the middle of an edge, and zero value at the other nodes located at the middle of the other edges. The polynomials P^1_1, P^1_2, P^1_3 of Eq. (12) are orthogonal:

$$\left(\int_{\mathrm{el}} P_i P_j = 0, i \neq j \right)$$

and the mass matrix resulting from the integration at the left-hand side of Eq. (7) is diagonal. For the first- as well as for the higher-order bases all calculations of Eq. (7), except the numerical flux evaluation, are carried out on the reference element. The numerical flux computation along the edges of the element, which depends on the neighboring element, is carried out at the physical space. Use of the orthogonal Jacobi polynomial basis $[P^1_1 = 1,\ P^1_2 = (3y + 1)/2,\ P^1_3 = 1 + 2x + y]$ yields the same computing cost. Reduced cost is achieved with the Lagrange nodal basis $P^1_1 = 1 - x - y$, $P^1_2 = x$, $P^1_3 = y$ for which only one polynomial is nonzero on each edge.

2. *Third-Order Polynomials*

The following first-order basis $P^3_{j=1,\ldots,10}$ is used to achieve fourth-order accuracy:

$$P^3_1 = 9x\left(x^2 - x - \tfrac{2}{9}\right)\Big/2, \qquad P^3_2 = 9y\left(y^2 - y - \tfrac{2}{9}\right)\Big/2$$

$$P^3_3 = 9(1 - x - y)\left(\tfrac{2}{3} - x - y\right)\left(\tfrac{1}{3} - x - y\right)\Big/2$$

$$P^3_4 = 9xy(3x - 1)/2, \qquad P^3_5 = 27xy\left(y - \tfrac{1}{3}\right)\Big/2$$

$$P^3_6 = 27y(1 - x - y)\left(y - \tfrac{1}{3}\right)\Big/2$$

$$P^3_7 = 27y(1 - x - y)\left(\tfrac{2}{3} - x - y\right)\Big/2$$

$$P^3_8 = 27x(1 - x - y)\left(\tfrac{2}{3} - x - y\right)\Big/2$$

$$P^3_9 = 27y\left(x - \tfrac{1}{3}\right)(1 - x - y)\Big/2$$

$$P^3_{10} = 27xy(1 - x - y) \tag{13}$$

At the reference element, each of these polynomials (Fig. 2) takes unit value at one of the $\frac{1}{3}$-distance nodes and zero value at all other nodes. The third-order polynomials, P^3_j, $j = 1, \ldots, 10$, of Eq. (13) are nonorthogonal, and the mass matrix of Eq. (7) is computed using high-order-accurate Gauss–Radau integration. On edge e_1, $(x, y) \in \{[0, 1] \times 0\}$ among the polynomials of Eq. (13) only P^3_j, $j = 1, 3, 8, 9$ are nonzero. The orthogonal Jacobi base polynomials, which are nonzero on all edges, are

$$P^3_1 = 1, \qquad P^3_2 = (3y + 1)/2$$

$$P^3_3 = 1 + 2x + y, \qquad P^3_4 = (-1 + 2x + 5y)/2$$

$$P^3_5 = P^3_3(3 + 5y)/2, \qquad P^3_6 = \left[3\left(P^3_3\right)^2 - (1 - y)^2\right](3 + 5y)/4$$

$$P^3_7 = (-3 - 15y + 15y^2 + 35y^3)/4$$

$$P^3_8 = \left[3\left(P^3_3\right)^2 - (1 - y)^2(5 + 7x)\right]\Big/4$$

$$P^3_9 = P^3_3[1 + 18y + 21y^2]/4$$

$$P^3_{10} = \left[5\left(P^3_3\right)^3 - 6(1 + x)(1 - y)^2 + 3\right](1 + x)^3/2 \tag{14}$$

3. *Fifth-Order Polynomials*

Sixth-order-accurate solutions in two dimensions are obtained with a polynomial basis that contains $7!/(2!\,5!) = 21$ polynomials. These polynomials (or higher-order polynomials[31,32]) can be systematically defined through the use of triangular coordinates $x, y, t = 1 - x - y$. The general form of Lagrange interpolation in triangular coordinates is given by

$$P_L(x, y, t) = L_i(x) L_j(y) L_k(t) \tag{15}$$

where $L_m(x)$ are one-dimensional $(m - 1)$-order Lagrange polynomials[31] and $L = L(i, j, k)$ (Fig. 3) denotes the nodal index. For example, in Fig. 3 at the nodal index $L(2, 3, 3)$ the base polynomial is defined as

$$P_{(2,3,3)}(x, y, t) = 5x \frac{y(y - 1/5)}{(2/25)} \frac{t(t - 1/5)}{(2/25)} \tag{16}$$

The fifth-order polynomial basis is also nonorthogonal, and the mass matrix is computed using Gauss–Radau integration. Note that the P^1_j and P^3_j nodal Lagrange bases can be constructed using the procedure followed for the construction of the P^5_j basis.

The nodal base was selected for sixth-order-accurate solutions with triangular elements because it yields reduced computing cost for the line integral of Eq. (7) compared to the modal, orthogonal bases and the nonorthogonal hierarchical (power) bases. The hierarchical power bases are more appropriate for multigrid.[24] Note, however, that the more general, orthogonal Jacobi polynomial bases[32] are hierarchical. Therefore for high-order-accurate solutions with multigrid the Jacobi polynomial bases could offer an advantage over the power base.

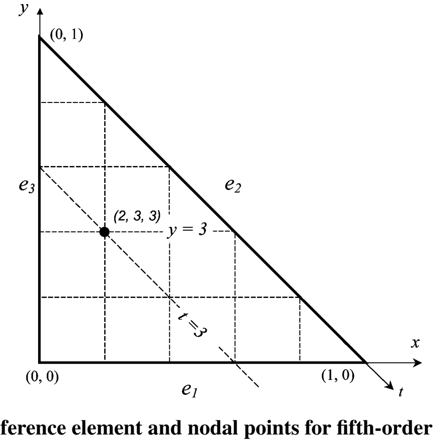

Fig. 3 Reference element and nodal points for fifth-order polynomial basis.

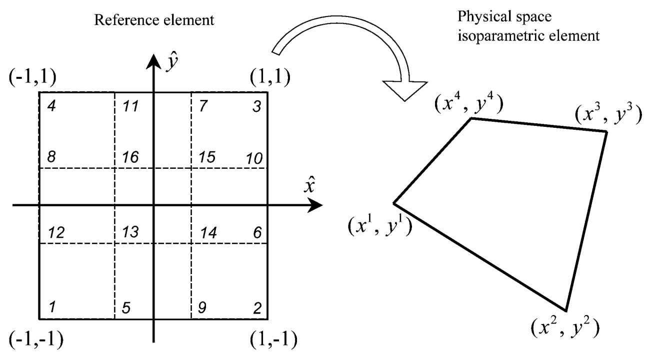

Fig. 4 Reference element with nodal points for third-order polynomial basis and isoparametric mapping for the arbitrary shape quadrilateral element in physical space.

C. Quadrilateral Element Bases

Space discretization was in addition obtained using quadrilateral isoparametric elements (Fig. 4) of arbitrary shape. The reference element is a square (Fig. 4) with vertices at the points $(-1, -1)$, $(1, -1)$, $(1, 1)$, $(-1, 1)$. In Fig. 4, the physical space arbitrary shape quadrilateral and the nodal points of the third-order-accurate polynomial basis on the reference element are also shown. The coordinates x_j^k; $j = 1, 2$; $k = 1, 2, 3, 4$ $(x_1^k = x^k, x_2^k = y^k)$ of the arbitrary shape quadrilateral elements in the physical space are related to the square reference element coordinates $\hat{x}_j$ $(\hat{x}_1 = \hat{x}, \hat{x}_2 = \hat{y})$ through the map

$$x_j = \sum_{k=1}^{4} \hat{f}_k(\hat{x}_1, \hat{x}_2) x_j^k \tag{17}$$

where $\hat{f}_k(\hat{x}_1, \hat{x}_2)$ are first-order Lagrange polynomials $\hat{f}_k(\hat{x}_1, \hat{x}_2) = (1 + x_1^k \hat{x}_1)(1 + x_2^k \hat{x}_2)/4$. The basis polynomials $P_i^k(x, y) \in Q^k$ for finite element discretization with quadrilateral elements are tensor products of appropriate order one-dimensional Lagrange, Legendre, or Jacobi polynomials. For example, the basis with third-order-accurate polynomials is $P_i^3(x, y) = L_j(x) L_k(y)$; $i = 1, \ldots, 16$; $j, k = 1, 2, 3, 4$.

V. Results

Second-, fourth-, and sixth-order-accurate numerical solutions for triangular meshes are computed using polynomial base functions P^1, P^3, and P^5, respectively. The accuracy of the numerical solutions is evaluated by comparing the computed results with exact solutions. The first test problem with an exact solution[33] is propagation and reflection from a solid wall of a Gaussian pressure pulse given by $p(x, y) = \exp\{-\ln 2[x^2 - (y - y_0)^2]/W\}$, where W is the width of the pulse and y_0 is the distance from the wall. The second problem with an exact solution is scattering of a similar Gaussian pressure pulse from the surface of a cylinder.[34]

The solution computed with third-order polynomial basis on a relatively coarse, fully unstructured mesh is shown in Fig. 5. At the far-field boundaries, the radiation boundary condition[2] given in Eq. (9) was used. It can be seen that the pressure waves exit the computational domain undistorted and there are no reflections in the interior from the computational boundaries. For convenience, evaluation of the numerical method is performed, on triangular meshes obtained from triangulation of structured Cartesian-type grids. The elements for the solution of Fig. 6 follow a uniform triangular-mesh generating pattern. It was shown in Ref. 18 that the accuracy of the computed solution depends on the triangular-mesh generating pattern. Comparing the computed solutions of Figs. 5 and 6, it appears that the coarse, canonical grid solution $(\Delta x = 2)$ obtained with the third-order P^3 polynomial basis shows some bias and more distortion than the fully unstructured mesh of Fig. 5 that has comparable resolution. Acoustic disturbance propagation is isotropic and does not require use of meshes with pattern,[18] and it appears that the unstructured mesh of Fig. 5 is more appropriate for acoustic wave propagation. The upper part of Fig. 6 shows, however, that for fine grids and high-order accuracy the bias introduced by the triangular-mesh generating pattern is very small. This is again consistent with the theoretical analysis of Ref. 18.

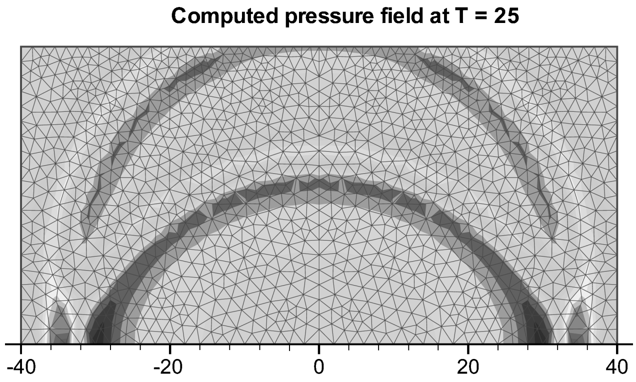

Fig. 5 Solution computed with an unstructured, triangular mesh and third-order polynomial basis.

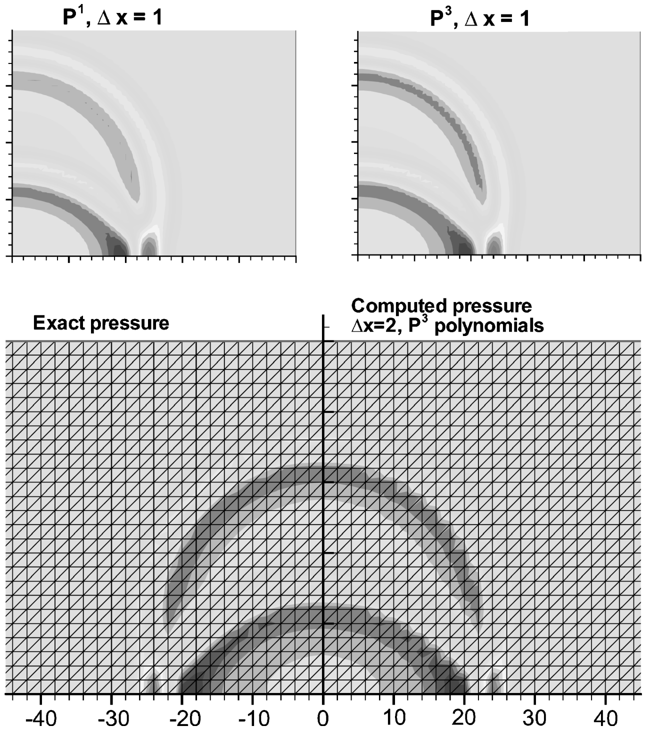

Fig. 6 Comparison of the pressure field computed with $\Delta x = 2$ triangular elements and third-order polynomial basis (right) with the exact solution (left).

Comparisons of computed solutions, using P_j^3 bases, with and without freestream at $T = 10$ are shown in Fig. 7. The presence of freestream does not interfere with the accuracy of the computed solution. The numerical solution with freestream $(M_x = 0.5)$ of Fig. 7 shows the same good agreement with the exact result obtained in Fig. 6 for propagation without freestream. The presence of the freestream results into a shift $(L_x = M_x T)$ of the wave pattern along the x direction. Furthermore, as expected, second- and fourth-order-accurate results computed with the nodal (Lagrange) basis and the orthogonal modal basis had the same agreement with the exact solution. However, the fourth-order-accurate solution computed with the modal (Lagrange) basis required approximately 10% more computing time.

The solutions shown in the following paragraphs were computed with the nodal base expansion until final time $T = 25$ on triangular canonical meshes with mesh-generating pattern (Fig. 6).

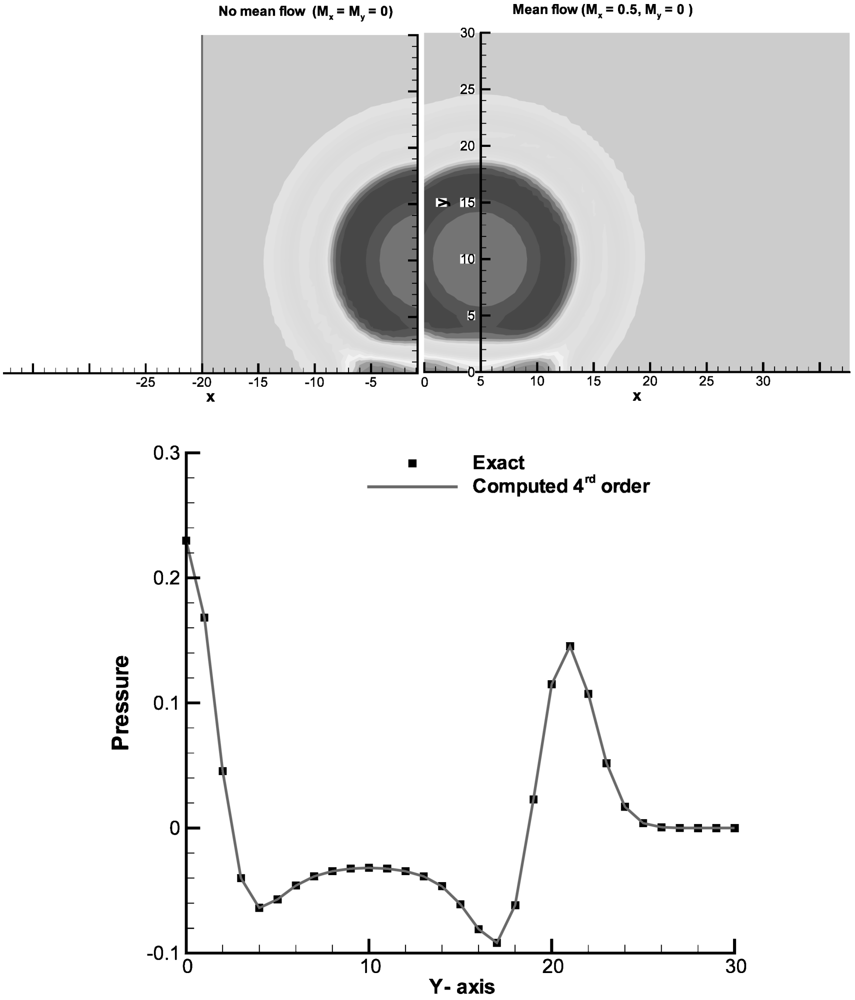

Fig. 7 Computed acoustic pressure field for propagation with ($M_x = 0.5$) and without ($M_x = 0.0$) freestream and comparison with the exact result at $T = 10$ for pulse propagation with freestream ($M_x = 0.5$).

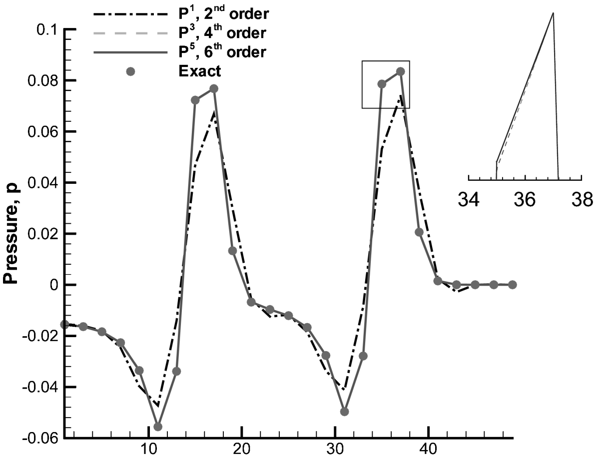

Fig. 8 Comparison of the pressure computed with P^1, P^3, and P^5 polynomial bases with the exact solution; in all cases the same canonical triangular mesh with $\Delta x = 2.0$ is used.

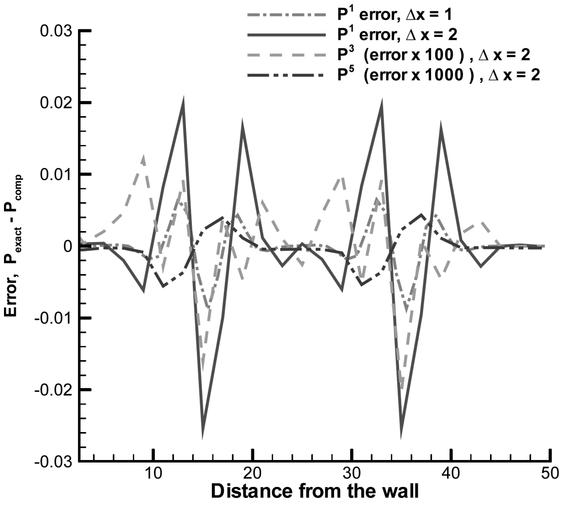

Fig. 9 Error of the solutions computed with P^1, P^3, and P^5 polynomial bases and canonical triangular meshes with $\Delta x = 2$.

Comparisons are carried out with the exact solution given in Ref. 33. A comparison of the solutions computed with grid spacing $\Delta x = 2.0$ is only shown in Fig. 8 because within plotting accuracy for $\Delta x = 1.0$ the differences between the fourth- and sixth-order-accurate solutions are not visible. The same time step $\Delta t = 0.01$, which is below the stability limit of the Runge–Kutta method was used for all solutions. The comparison with the exact result of Ref. 33 is shown along the symmetry line, which is normal to the wall at $x = 0$. For the same location, the error $\varepsilon_r = (p_{\text{com}} - p_{\text{ex}})$ of the computed solutions is shown in Fig. 9. Clearly, only for $\Delta x < 1.0$ do the results computed with the first-order polynomial basis (second-order accurate solutions) provide the accuracy level needed in aeroacoustic computations. Computations with so fine meshes become time consuming especially in three dimensions. Therefore a high order of accuracy (at least fourth order) is needed to reduce computing times.

In Fig. 10, the grid convergence of the second-, fourth-, and sixth-order-accurate solutions is shown. The error norm in Fig. 10 was computed on the symmetry line, where the error norm is expected to be the largest, and not for the entire domain. Norms of the error computed in the full domain do not differ much from the error norm obtained from the deviation of the computed solution from the exact result only on the symmetry line. In both cases, the error norm was computed from

$$L_2 = \left\{ \frac{1}{N_{\mathrm{el}}} \sum_{\mathrm{el}=1}^{N_{\mathrm{el}}} \int_{\mathrm{el}} [p_{\mathrm{comp}}(x, y, t) - p_{\mathrm{exact}}(x, y, t)]^2 \right\}^{\frac{1}{2}} \tag{18}$$

The grid convergence plot of Fig. 10 shows that all solutions achieve the expected order of accuracy. Once again it is evident that the desired order of accuracy for CAA can only be achieved with higher-order methods. Furthermore, it was found that for this simple problem the solution computed with fourth- or sixth-order accuracy and single precision practically converges when $\Delta x \simeq 1.0$, and the remaining errors are mainly as a result of time integration. In Fig. 11, the reduction of the average error is plotted vs the required computing time for the solution. It can be seen that use of

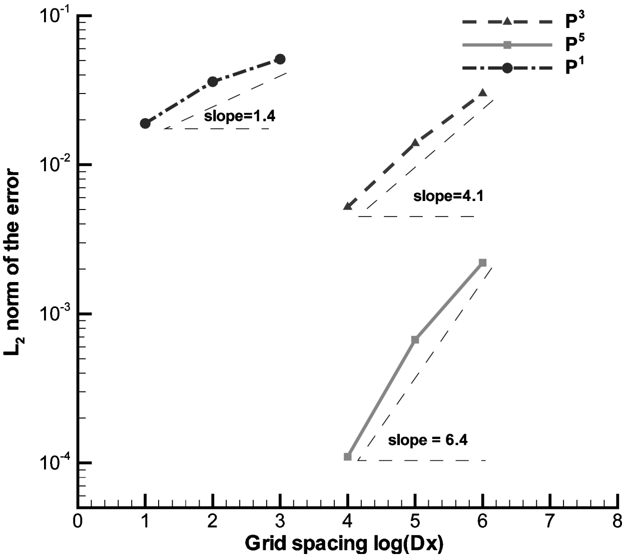

Fig. 10 Grid convergence (in the L_2 norm of the computed pressure) of the second-order (P^1)-, the fourth-order (P^3)-, and sixth-order (P^5)-accurate solutions computed with triangular elements.

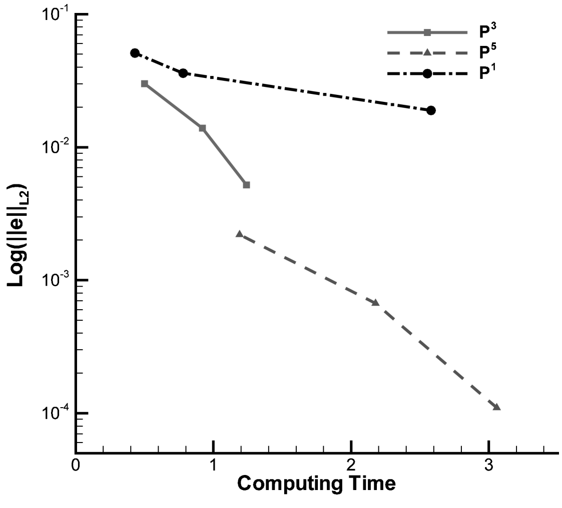

Fig. 11 Computing time required in order to achieve certain error level (L_2 error norm of the computed pressure) with second-order (P^1)-, fourth-order (P^3)-, and sixth-order (P^5)-accurate solutions.

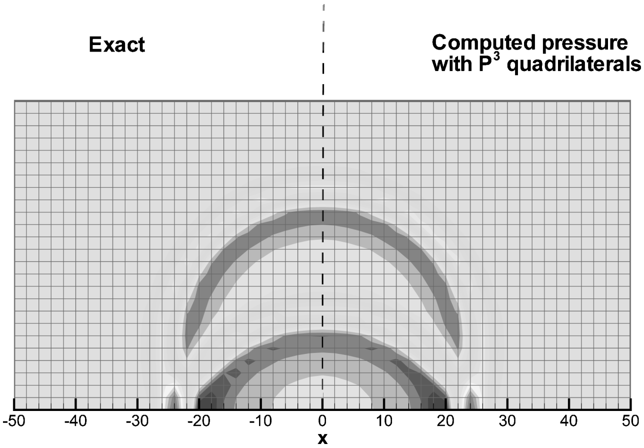

Fig. 12 Comparison of the pressure field computed with quadrilateral elements $\Delta x = 2$ and third-order polynomial basis with the exact solution.

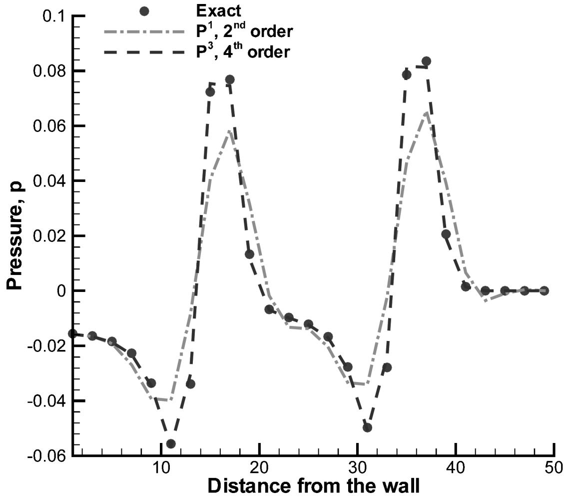

Fig. 13 Comparison of pressure field computed with quadrilateral canonical meshes and P^1, P^3 polynomial bases with the exact solution.

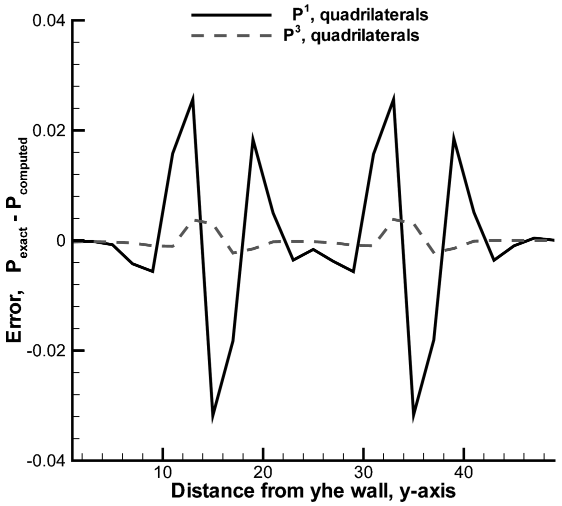

Fig. 14 Error of the solutions computed with P^1 and P^3 polynomial bases on quadrilateral meshes; in both cases canonical quadrilateral meshes $\Delta x = 2.0$ are used.

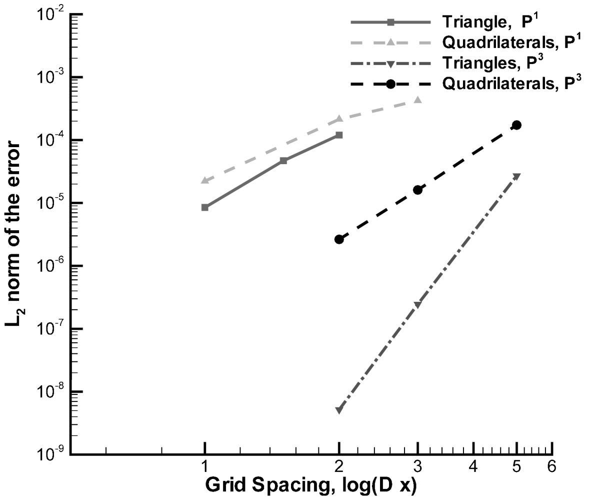

Fig. 15 Comparison of the grid convergence (in the L_2 norm of the computed pressure) of solutions computed with triangular and quadrilateral elements.

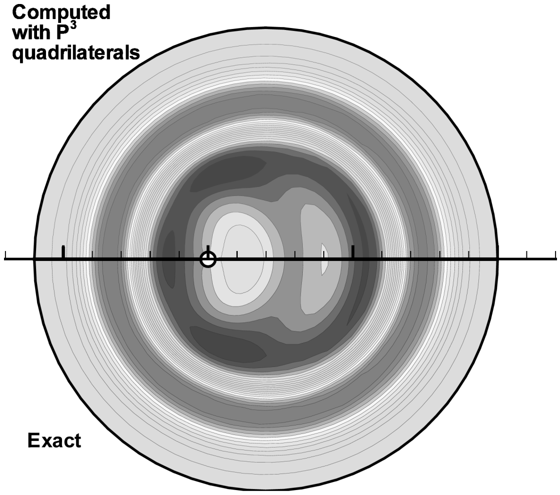

Fig. 16 Comparison of the computed pressure field obtained with P^3 quadrilateral elements with the exact solution for scattering from a cylinder surface.

higher-order accuracy yields savings in computing time when the solution must reach certain error level.

Solutions computed with quadrilateral meshes are presented next. A comparison of the pressure field computed with third-order polynomial basis with the exact result is shown in Fig. 12. It can be seen (compare Figs. 6 and 12) that for equivalent grid resolution the quadrilateral mesh yields better isotropy of the computed solution. The deviations of the computed solutions with first- and third-order polynomial bases from the exact result are shown in Fig. 13. The error of the computed solutions from the exact result on the symmetry line is shown in Fig. 14. The grid convergence of the solutions computed with quadrilateral elements is shown in Fig. 15. For comparison, the convergence achieved with solutions computed with triangular elements is shown in the same plot. It appears that the solutions computed with quadrilateral elements do not quite achieve the $(k+1)$th order of accuracy observed for triangular elements. This is expected because in a computation with third-order basis, for example, the unit area (for $\Delta x = \Delta y = 1$) is spanned by 16 polynomials in quadrilateral elements, whereas for triangular element discretization the same area is covered by two elements and spanned by 20 ($2 \times P^3_{j=1,\ldots,10} = 20$) polynomials. In terms of computing time, the solution of obtained with quadrilateral elements requires slightly less computing time.

Solutions for more complex domains are presented next. First, scattering of sound waves from the surface of a cylinder, which is one of the benchmark problems of Ref. 34, is considered. The computed solution with third-order polynomial basis and quadrilateral elements at $T = 8$ is compared with the exact result in Fig. 16. Very good agreement with exact result is achieved for the solutions computed with both triangular and quadrilateral elements. The computational domain for the solution obtained with triangular elements contains 5437 elements or 2810 vertices. Discretization of the same domain with isoparametric quadrilaterals includes 2000 elements or 2091 vertices. In both cases the cylinder was represented by 40 elements. A comparison of the computed pressure at $T = 5$ that is obtained with the triangular element solution for selected radial directions ($\phi = 0$ and 90 deg) with the exact result is shown in Fig. 17. The computed solution along the radial direction was interpolated from surrounding nodes. The interpolated computed solution is in good agreement with the exact result. The time variation of the computed solution for $0 \le T \le 8$ is shown in Fig. 18. Again good agreement with the exact result[34] is achieved.

Next, scattering of a Gaussian pulse with variable in time amplitude from the surfaces of two cylinders with different diameters is

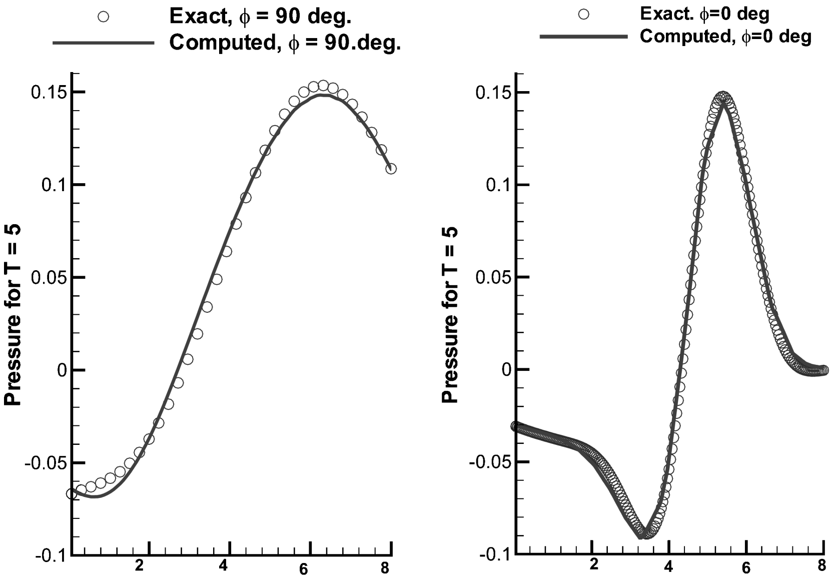

Fig. 17 Comparison of the computed pressure at final time $T = 5$ for $\phi = 0$ and 90 deg with the exact solution for pulse scattering.

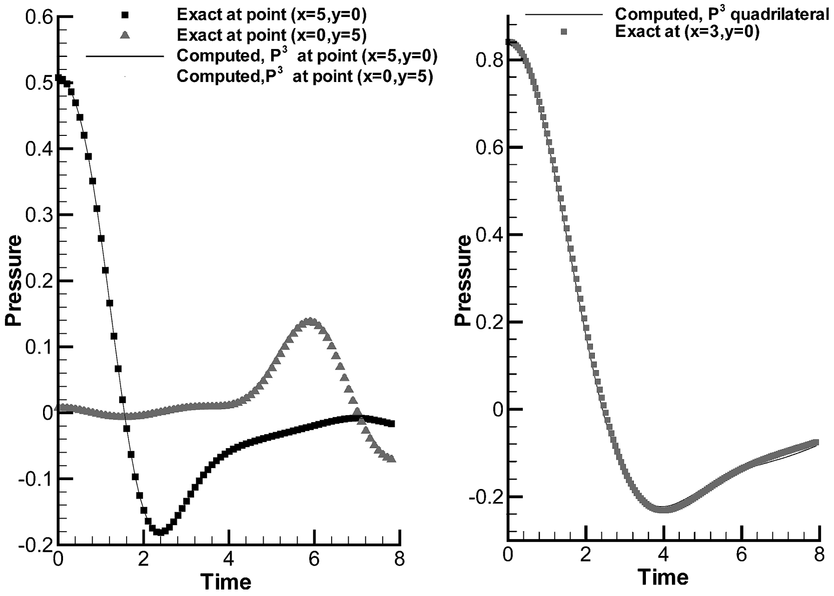

Fig. 18 **Comparison of the computed pressure at $r = 5.0$ and $0 \leq T \leq 8$ for $\phi = 0$ and 90 deg with the exact solution for pulse scattering.**

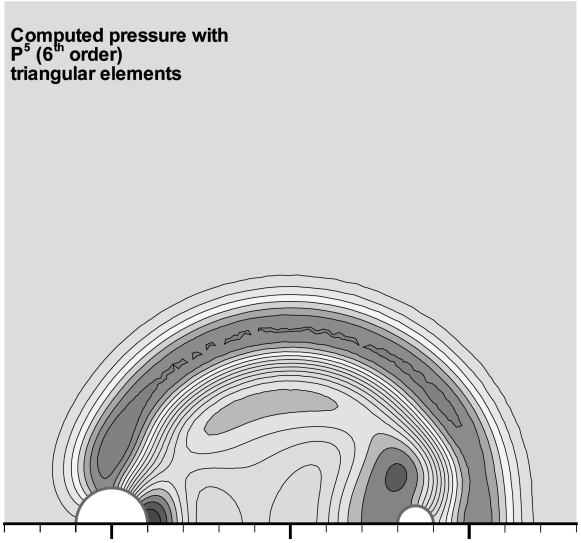

Fig. 19 **Computed pressure field with triangular mesh and P^5 polynomial basis for scattering of a pressure pulse from the surfaces of two cylinders.**

considered. The large cylinder has diameter $D_1 = 2$, and the small cylinder has diameter $D_2 = 1$. The distance between the centers is $8.5D_2$, the large cylinder center is at $(-5, 0)$, the small cylinder center is at (3.5, 0), and the source is located at (0, 0). The solution is computed using triangular elements because the meshing of the domain with triangular elements is easier and the resulting mesh is more isotropic. The surface of the large cylinder is represented by 40 elements, and the surface of the small cylinder is represented by 20 elements. The entire domain contains 7671 elements or 3929 vertices, and the solution is obtained with the P^5 polynomial basis. The computed pressure field at time $T = 10$ is shown in Fig. 19.

Numerical solutions obtained with the DG finite element method for benchmark aeroacoustic problems demonstrated that only P^3 (fourth-order) or higher-order-accurate discretizations provide the required reslution for CAA. All of the results presented were computed on a single PC-linux processor using single-precision arithmetic. In terms of computing time, solutions with equivalent order of accuracy obtained on triangular meshes require about 10% more resources than the solutions obtained with quadrilateral meshes. In both cases, the Courant–Friedrichs–Lewy stability limitations become more stringent, compare Ref. 20 with the increase of the order of spatial accuracy. For isotropic meshes, the resolving ability of both triangular and quadrilateral space discretizations is approximately equivalent. For two-dimensional problems, it is feasible to achieve spatial accuracy up to sixth order. Sixth or higher order of accuracy is possibly advantageous for long time propagation of complex waveforms. Numerical tests for pure convection ($u_t + u_x = 0$) of complex one-dimensional waves of the form $u(x; t = 0) = [2 + \cos(\alpha x)]\exp[-\ln 2(x/10)^2]$, $\alpha = 1.7$, using up to 10th-order-accurate DG discretizations showed that for long time integration ($T > 400$) at least sixth-order accuracy is needed.

Extension of the DG method for three-dimensional CAA applications is straightforward using the available finite element framework[31] but beyond the scope of the present paper. It appears that three-dimensional CAA applications with the DG method are feasible in terms of the required computing resources; however, global discretizations with polynomial bases of order higher than three are possibly too intensive computationally. Therefore, in three-dimensional applications some type of adaptive p refinement[32] must be applied to reduce the computing cost associated with high-order polynomial bases. The p-adaptive schemes for aeroacoustic computations could be based only on the gradient of the computed pressure, and they are more straightforward to apply compared to adaptive schemes for the full inviscid flow equations.[35]

VI. Conclusions

High-order-accurate numerical solutions of the linearized Euler equations were obtained using the discontinuous Galerkin finite element method for general, unstructured-type, triangular and quadrilateral meshes. The accuracy of the numerical solutions was verified by comparing with available exact results. Grid convergence to the theoretical $(k + 1)$th order of accuracy for order k polynomial basis was achieved for triangular element discretizations. It appears that fourth- and sixth-order-accurate solutions provide sufficient accuracy for two-dimensional CAA computations. The versatility of the numerical solution is demonstrated with complex domain numerical solutions for scattering from a cylinder surface and computation of scattering from the surfaces of two cylinders. It is estimated that extension of the method to three dimensions is feasible with the available computing resources.

Acknowledgment

This effort was sponsored by the Air Force Office of Scientific Research, Air Force Material Command, U.S. Air Force, under Grant FA8655-03-1-3085.

References

[1] Lele, S. K., "Compact Finite Difference Schemes with Spectral-Like Resolution," *Journal of Computational Physics*, Vol. 103, No. 1, 1992, pp. 16–42.

[2] Tam, C. K., and Webb, J. C., "Dispersion-Relation Preserving Finite Difference Schemes for Computational Acoustics," *Journal of Computational Physics*, Vol. 107, No. 2, 1993, pp. 262–281.

[3] Wang, Z. J., and Chen, R. F., "Optimized Weighted Essentially Non-Oscillatory Schemes for Linear Waves with Discontinuity," *Journal of Computational Physics*, Vol. 174, No. 1, 2001.

[4] Grasso, F., and Pirozzoli, S., "Simulations and Analysis of the Coupling Process of Compressible Vortex Pairs; Free Evolution and Shock Induced Coupling," *Physics of Fluids*, Vol. 13, No. 5, 2001, pp. 1343–1366.

[5] Visbal, M. R., and Gaitonde, D. V., "On the Use of High-Order Finite-Difference Schemes on Curvilinear and Deforming Meshes," *Journal of Computational Physics*, Vol. 181, No. 1, 2002, pp. 155–185.

[6] Hixon, R., "Curvilinear Wall Boundary Conditions for Computational Aeroacoustics," AIAA Paper 99-2395, June 1999.

[7] Hixon, R., "Effect of Grid Singularities on the Solution Accuracy of a CAA Code," AIAA Paper 2003-0879, Jan. 2003.

[8] Gaitonde, D. V., and Visbal, M. R., "Pade-Type High-Order Boundary Filters for the Navier–Stokes Equations," *AIAA Journal*, Vol. 38, No. 11, 2000, pp. 2103–2112.

[9] Jiang, G.-S., and Shu, C.-W., "Efficient Implementation of Weighted ENO Schemes," *Journal of Computational Physics*, Vol. 126, No. 1, 1996, pp. 202–228.

[10] Balsara, D. S., and Shu, C.-W., "Monotonicity Preserving Weighted Essentially Non-Oscillatory Schemes with Increasingly High Order of Accuracy," *Journal of Computational Physics*, Vol. 160, No. 2, 2000, pp. 405–452.

[11] Pirozzoli, S., "Conservative Hybrid Compact-WENO Schemes for Shock Turbulence Interaction," *Journal of Computational Physics*, Vol. 178, No. 1, 2002, pp. 81–117.

[12] Ekaterinaris, J. A., "Performance of High-Order-Accurate, Low-Diffusion Numerical Schemes for Compressible Flow," *AIAA Journal*, Vol. 42, No. 3, 2004, pp. 493–500.

[13] Abgral, R., "On Essentially Non-Oscillatory Schemes on Unstructured Meshes," *Journal of Computational Physics*, Vol. 114, No. 1, 1994, pp. 45–58.

[14] Cockburn, B., Karniadakis, G. E., and Shu, C.-W. (eds.), *Discontinuous Galerkin Methods*, Springer, Berlin, 1999.

[15] Wang, Z. J., "High-Order Spectral Volume Method for Benchmark Aeroacoustic Problems," AIAA Paper 2003-0880, Jan. 2003.

[16] Yan, J., and Shu, C.-W., "Local Discontinuous Galerkin Methods for Partial Differential Equations with Higher Order Derivatives," NASA CR-2002-211959 and ICASE Rept. 2002-42, Nov. 2002.

[17] van der Veght, J. J. W., and van der Ven, H., "Space–Time Discontinuous Galerkin Finite Element Method with Dynamic Grid Motion for Inviscid Compressible Flows: I. General Formulation," *Journal of Computational Physics*, Vol. 182, No. 2, 2002, pp. 546–585.

[18] Hu, F. Q., Hussaini, M. Y., and Rasetarinera, P., "An Analysis of the Discontinuous Galerkin Method for Wave Propagation Problems," *Journal of Computational Physics*, Vol. 151, No. 2, 1999, pp. 921–946.

[19] Hu, F. Q., and Atkins, H. L., "Eigensolution Analysis of Discontinuous Galerkin Method with Non-Uniform Grids, Part I: One Space Dimension," *Journal of Computational Physics*, Vol. 182, No. 1, 2002, pp. 516–564.

[20] Atkins, H. L., and Shu, C.-W., "Quadrature-Free Implementation of Discontinuous Galerkin Method for Hyperbolic Problems," *AIAA Journal*, Vol. 36, No. 5, 1998, pp. 775–782.

[21] Ozdemir, H., Blom, C. P. A., Hagmeijer, R., and Hoeijmakers, H. W. M., "Development of Higher-Order Discontinuous Galerkin Method on Hexahedral Elements," AIAA Paper 2004-2961, May 2004.

[22] Pierce, A. D., *Acoustics; An Introduction to the Physical Principles and Applications*, McGraw–Hill, 1981.

[23] Rasetarinera, P., and Hussaini, M. Y., "An Efficient Implicit Discontinuous Spectral Galerkin Method," *Journal of Computational Physics*, Vol. 172, No. 2, 2001, pp. 718–738.

[24] Fidkowski, K. J., and Darmofal, D. L., "Development of a Higher-Order Solver for Aerodynamic Applications," AIAA Paper 2004-0436, Jan. 2004.

[25] Hu, F. Q., Hussaini, M. Y., and Manthey, J. L., "Low-Dissipation and Low-Dispersion Runge–Kutta Schemes for Computational Acoustics," *Journal of Computational Physics*, Vol. 124, No. 1, 1996, pp. 177–191.

[26] Hixon, R., and Turkel, E., "Compact Implicit MacCormack-Type Schemes with High Accuracy," *Journal of Computational Physics*, Vol. 158, No. 1, 2000, pp. 51–70.

[27] Gottlieb, S., and Shu, C.-W., "Total Variation Diminishing Runge–Kutta Schemes," *Mathematics of Computation*, Vol. 67, No. 221, 1998, pp. 73–85.

[28] Reed, W. H., and Hill, T. R., "Triangular Mesh Methods for the Neutron Transport Equation," Los Alamos Scientific Lab., TR LA-UR-73-479, Los Alamos, NM, 1973.

[29] Cockburn, B., and Shu, C.-W., "The Runge–Kutta Local Projection Discontinuous Galerkin Finite Element Method for Conservation Laws IV: The Multidimensional Case," *Mathematics of Computation*, Vol. 54, 1990, pp. 545–581.

[30] Cockburn, B., and Shu, C.-W., "The Runge–Kutta Discontinuous Galerkin Method for Conservation Laws," *Journal of Computational Physics*, Vol. 141, No. 2, 1998, pp. 199–224.

[31] Hughes, T. J., *The Finite Element Method*, Prentice–Hall, Upper Saddle River, NJ, 1987.

[32] Karniadakis, G. E., and Sherwin, S. J., *Spectral/hp Elemnt Method for CFD*, Numerical Mathematics in Scientific Computation, Oxford Univ. Press, New York, 1999.

[33] Hardin, J. C., Ristorcelli, J. R., and Tam, C. K., *ICASE/LaRC Workshop on Benchmark Problems in Computational Aeroacoustics (CAA)*, NASA CP 3300, 1995.

[34] Tam, C. K. W., and Hardin, J. C., "Second Computational Aeroacoustics (CAA) Workshop on Benchmark Problems," NASA CP 3352, Nov. 1997.

[35] Van der Vegt, J. J. W., and Van der Ven, H., "Space Time Discontinuous Galerkin Finite Element Method with Dynamic Grid Motion for Inviscid Compressible Flows: I. General Formulation," *Journal of Computational Physics*, Vol. 182, No. 2, 2002, pp. 546–585.

K. Fujii
Associate Editor